The Astrophysical Journal, 927:3 (8pp), 2022 March 1 https://doi.org/10.3847/1538-4357/ac4af1

Investigating the Accretion Nature of Binary Supermassive Black Hole Candidate SDSS J025214.67−002813.7

Adi Foord[1], Xin Liu[2,3], Kayhan Gültekin[4], Kevin Whitley[4], Fangzheng Shi[2], and Yu-Ching Chen[2,3,5]
[1] Kavli Institute of Particle Astrophysics and Cosmology, Stanford University, Stanford, CA 94305, USA
[2] Department of Astronomy, University of Illinois at Urbana-Champaign, Urbana, IL 61801, USA
[3] National Center for Supercomputing Applications, University of Illinois at Urbana-Champaign, Urbana, IL 61801, USA
[4] Department of Astronomy and Astrophysics, University of Michigan, Ann Arbor, MI 48109, USA
[5] Center for AstroPhysical Surveys, National Center for Supercomputing Applications, Urbana, IL, 61801, USA
Received 2021 October 5; revised 2021 December 27; accepted 2022 January 11; published 2022 March 2

Abstract

We present results of a multiwavelength analysis of SDSS J025214.67−002813.7, a system that has been previously classified as a binary active galactic nucleus (AGN) candidate based on periodic signals detected in the optical light curves. We use available radio−X-ray observations of the system to investigate the true accretion nature. Analyzing new observations from XMM-Newton and NuSTAR, we characterize the X-ray emission and search for evidence of circumbinary accretion. Although the 0.5–10 keV spectrum shows evidence of an additional soft emission component, possibly due to extended emission from hot nuclear gas, we find the spectral shape is consistent with that of a single AGN. Compiling a full multiwavelength spectral energy distribution (SED), we also search for signs of circumbinary accretion, such as a "notch" in the continuum due to the presence of minidisks. We find that the radio–optical emission agrees with the SED of a standard, radio-quiet, AGN; however, there is a large deficit in emission blueward of ∼1400 Å. Although this deficit in emission can plausibly be attributed to a binary AGN system, we find that the SED of SDSS J0252−0028 is better explained by emission from a reddened, single AGN. However, future studies of the expected hard X-ray emission associated with binary AGNs (especially in the unequal-mass regime) will allow for more rigorous analyses of the binary AGN hypothesis.

Unified Astronomy Thesaurus concepts: Active galactic nuclei (16); High energy astrophysics (739); Galaxy mergers (608); Black hole physics (159); X-ray astronomy (1810); X-ray active galactic nuclei (2035)

1. Introduction

A binary supermassive black hole (SMBH) represents the final stage of a galaxy merger, where the two massive host galaxies have likely been interacting for hundreds of megayears to gigayears (Begelman et al. 1980). The merging system is classified as a binary when the SMBHs are gravitationally bound in a Keplerian orbit, and for a wide range of SMBH masses and host galaxy environments this occurs at orbital separations of <10 pc (Dotti et al. 2007; Mayer et al. 2007; Khan et al. 2012). The fate and final coalescence of the system strongly depends on the amount of matter the SMBHs can interact with (Merritt et al. 2007; Sesana et al. 2007). As the last stage before coalescence, binary SMBHs represent an observable link between galaxy mergers and gravitational-wave events. They are strong emitters of low-frequency gravitational waves, which are expected to dominate the gravitational-wave background signal detected by pulsar timing arrays (PTAs; Burke-Spolaor et al. 2019), and they are direct precursors to gravitational-wave events detectable by future space-based laser interferometers (Sesana et al. 2007; Luo et al. 2016).

Currently, detections of binary SMBHs are limited to systems where both black holes are actively accreting (active galactic nuclei, or AGNs) and emitting light across the electromagnetic spectrum. Given the small physical separations between the two SMBHs, the angular resolution afforded by radio interferometry is required to spatially resolve binary AGN systems, such as in the serendipitous discovery of 0402+379 (Rodriguez et al. 2006). However, radio detections of binary AGNs remain limited to relatively low redshifts (where separations below 1 pc can only be probed up to $z = 0.1$) and systems with two radio-bright AGNs (where only ∼15% of AGNs are expected to be radio loud; see, e.g., Hooper et al. 1995; Kellermann et al. 2016). On top of this, blind surveys with very long baseline interferometry (VLBI) networks are limited by the narrow (∼arcsecond-scale) fields of view. As a result, the number of confirmed binary AGNs remains small.

Given the difficulty associated with directly detecting binary AGNs, many indirect detection techniques are used to search for the elusive systems. One of the most popular methods is to identify quasars with photometric variability, and in particular, periodic signals in their light curves. Periodicity in light curves may arise for various reasons, such as jet precession (where the presence of a companion can introduce a periodicity in the velocity of an otherwise straight jet; see Hardee et al. 1994; Deane et al. 2014), the dynamics of a secondary periodically intercepting the primary SMBH's accretion disk (i.e., OJ 287; see Valtonen et al. 2008 and the recent review in Dey et al. 2019), or accretion via a circumbinary disk (Hayasaki et al. 2007; MacFadyen & Milosavljević 2008; Roedig et al. 2012; D'Orazio et al. 2013; Farris et al. 2014; Roedig et al. 2014; Muñoz et al. 2020). Recently, systematic scans of large areas of the sky carried out via time-domain surveys allow for statistical searches for periodic variability in large samples of quasars (Valtonen et al. 2008; Graham et al. 2015; Bon et al. 2016; Charisi et al. 2016; Li et al. 2016; Liu et al. 2019; Chen et al. 2020). Such analyses are complicated by the fact that AGN light curves are characterized by stochastic, red noise variability; it has been shown that this red noise can be misidentified as a periodic signal with time baselines of fewer than five periods (Vaughan et al. 2016). Although these

surveys have collectively found over 100 binary AGN candidates, to date there are no confirmed binary AGNs with separations at the submilliparsec scale.

A different approach is to use available multiwavelength observations to search for evidence of circumbinary accretion (see, e.g., Foord et al. 2017). Circumbinary accretion is expected at small separations (when the typical accretion disk size is larger than the binary separation a; Milosavljević & Phinney 2005). Here, two accretion disks around each SMBH ("minidisks") are surrounded by a larger, circumbinary accretion disk. The minidisks extend to a tidal truncation radius (i.e., where the tidal torques of the disks balance the viscous torque of the circumbinary accretion disk), where values are less than $a/2$ (Paczynski 1977, but see Roedig et al. 2014 for how the radius depends on the mass ratio of the system). In later stages, the angular momentum of the innermost stable orbit (ISCO) of the SMBHs may exceed that of the material falling from the circumbinary accretion disk; in this scenario there will be no minidisks, as material will fall directly into each SMBH (see Gültekin & Miller 2012; Tanaka & Haiman 2013; Gold et al. 2014; Roedig et al. 2014). Each accretion scenario will manifest differently in the spectral energy distribution (SED) of a binary AGN, where dips in the optical—UV bands or very little high-energy emission is observed (see Roedig et al. 2014; Foord et al. 2017). Complications to these simple scenarios naturally arise when accounting for stream shocking, or when supersonic material from the circumbinary accretion disk hits the outer edge of the minidisks. The high-energy signal associated with these types of events can wash out any dip in the optical regime of the SED (Roedig et al. 2014; Farris et al. 2015a, 2015b). This is especially true for systems where the dips in emission are expected to be subtle with respect to the overall shape of the SED (which depend on the mass ratio between the secondary and primary SMBH and the accretion rates of each SMBH; see Section 3 for more details).

Here, we present a multiwavelength analysis of binary AGN candidate SDSS J025214.67−002813.7 (hereafter SDSS J0252−0028), located at $z = 1.53$. It has an estimated virial black hole mass of $M = 10^{8.4\pm0.1}\,M_{\odot}$, a physical separation on the order of ≈4 milliparsecs (or 200 Schwarzschild radii), and a binary mass ratio on the order of ∼0.1 (Liao et al. 2021). SDSS J0252−0028 was part of a large systematic search for periodic light curves in 625 quasars via combining Dark Energy Survey Supernova (DES-SN) Y6 observations with archival Sloan Digital Sky Survey (SDSS) S82 data (Chen et al. 2020). Briefly, quasars were flagged as having significant periodicity in their light curves if (1) at least two photometric bands had a 3σ detection of the same periodicity in the periodogram analysis, (2) the detected periodicity was the dominant signal with respect to the background (red noise), and (3) the same periodicity was also identified in the autocorrelation function analysis (see Liao et al. 2021 for more details). Among the five quasars flagged as significant periodic candidates, SDSS J0252−0028 was the most significant detection based on ∼4.6 cycles detected over a 20 year long baseline. Recent X-ray observations via XMM-Newton and NuSTAR, along with available radio (Very Large Array; VLA), mid-infrared (Wide-field Infrared Survey Explorer; WISE), near-infrared (UKIRT Infrared Deep Sky Survey; UKIDSS), optical (SDSS), and UV (Galaxy Evolution Explorer; GALEX) observations, allow for a multiwavelength analysis to search for evidence of two SMBHs.

Our paper is organized in the following manner. In Section 2 we analyze new X-ray observation of SDSS J0252−0028 and evaluate the 0.5–10 keV spectrum for evidence of a binary AGN system; in Section 3 we present the multiwavelength SED and compare the emission to both single and binary AGN emission models; in Section 4 we discuss our results and test for effects of reddening; and in Section 5 we review our conclusions. We assume a standard ΛCDM cosmology of $\Omega_{\Lambda} = 0.7$, $\Omega_{M} = 0.3$, and $H_0 = 70$ km s^{-1} Mpc^{-1}.

2. X-Ray Observations

SDSS J0252−0028 was targeted by NuSTAR and XMM-Newton in a joint NuSTAR Cycle 6 Proposal (PI: Liu, ID: 6061). The quasar was observed for 100 and 50 ks with NuSTAR and XMM-Newton on 2020 August 30 (observation ID 60601009002) and 2020 August 02 UT (observation ID 0870810201). The NuSTAR exposure time was set to achieve at least ∼10 counts under the assumption of a typical optical quasar SED. The XMM-Newton exposure time was set to achieve ∼200 counts for a ∼10% flux measurement and a simultaneous fit to the X-ray spectral index within ±0.3 and the intrinsic hydrogen column density to an upper limit of $\sim10^{21}$ cm^{-2} (both at ∼90% confidence).

All errors evaluated in the following section are done at the 95% confidence level, and error bars quoted in the following section are calculated with Monte Carlo Markov Chains via the XSPEC tool `chain`.

2.1. NuSTAR

We follow the standard process *nupipeline* embedded in the software package NuSTARDAS v1.9.2 to clean the event file of the NuSTAR observation. We find no emission consistent with an X-ray point source within 100″ of the SDSS-listed optical center of SDSS J0252−0028. We calculate a 3σ upper limit for 3–10 keV and 10–79 keV fluxes of 8.8×10^{-14} erg s^{-1} and 67×10^{-14} erg s^{-1}, respectively, within a circular region with a radius of 100″ centered on the optical center.

2.2. XMM-Newton

We clean and process the XMM-Newton EPIC pn observation using the XMM-Newton Science Analysis System (SAS) software package v18.0.0 (Gabriel et al. 2004). The quasar's net count rate and flux value are determined using XSPEC, version 12.11.1 (Arnaud 1996). We generate the event list with the standard pipeline *epproc*. We filtered the event list from high-background time intervals and calculate a good exposure time of 42.59 ks. The quasar was identified as an X-ray point source coincident with the nominal SDSS-listed optical center of SDSS J0252−0028. Counts are extracted from a circular region with a radius of 32″ centered on the X-ray source center, using a source-free circular region with a radius of 90″ for the background extraction. The spectrum was been rebinned via the `specgroup` tool to ensure a minimum signal-to-noise ratio of 2 over the 0.3–10 keV band.

To characterize the X-ray emission and search for evidence of two accreting SMBHs, we fit the observed-frame 0.5–10 keV spectrum with three different model: Model 1, an absorbed redshifted power law (`phabs` × `zphabs` × `zpow`), and Models 2 and 3, an absorbed redshifted broken power law (`phabs` × `zphabs` × `zbknpow`), where the photon index values are tied for Model 2. We expect that Model 1 and Model

2 should return results consistent with one another; however, comparing Model 2 and Model 3 should allow us to test for the presence of two AGNs, which may be contributing X-ray emission from individual accretion disks (and thus two power-law photon indices may better describe the X-ray emission).

We implement the Cash statistic (cstat; Cash 1979) to best assess the quality of our model fits. In particular, we quantify whether one model is preferred over another by evaluating whether there is a statistically significant improvement in the fit, such that $\Delta C_{\rm stat} > \Delta N_{\rm fp} \times 2.71$ (where $\Delta N_{\rm fp}$ represents the difference in the number of free parameters between the models; Tozzi et al. 2006; Brightman & Ueda 2012), corresponding to a fit improvement with 90% confidence (Brightman et al. 2014). The use of Poisson statistics (i.e., the Cash statistic) when fitting X-ray spectral data has many strengths over χ^2 statistics. However, the principal disadvantage of the Cash statistic is that there is no value corresponding to the reduced χ^2 value, which allows one to measure the goodness of the fit. The $\Delta C_{\rm stat} > \Delta N_{\rm fp} \times 2.71$ criterion assigns the same confidence levels for Cash statistics as are defined for χ^2 statistics (i.e., $\Delta C_{\rm stat} = 2.7$ corresponds to 90% C.L. for one interesting parameter) and has been shown to be an appropriate assumption when modeling X-ray spectra (see Tozzi et al. 2006; Kaastra 2017). Similar to χ^2 statistics, the $\Delta C_{\rm stat}$ criterion we implement should be appropriate to use between nested models. *K*-corrections are not applied to the XMM-Newton data, as we directly measure the flux density from the spectrum.

As expected, we find that Model 1 and Model 2 return consistent results; but using the $\Delta C_{\rm stat}$ criterion stated above, we find that Model 3 results in a significant improvement in the fit compared to Model 2. However, the best-fit values for the power-law photon indices Γ_1 and Γ_2 are unconstrained and pegged to values consistent with the low ($\Gamma_1 \approx 1$) and high ($\Gamma_2 \approx 3$) end of the allowed range (where values less than 1 or greater than 3 are usually considered nonphysical; see Ishibashi & Courvoisier 2010). These results may indicate that the X-ray spectrum is consistent with emission from a single AGN, but requires additional components to a simple power law.

Thus, we add several additional components to the absorbed power law to test if they better describe the X-ray emission. In particular, we look at a partially covered power law (phabs × ((zphabs × zpow) +zpow), where the photon indices of each power law are tied; Model 4) and a power law with diffuse gas to account for possible extended soft X-ray emission in the nucleus (phabs × ((zphabs × zpow) +APEC), with abundance fixed at the solar value; Model 5). We find that the best-fit parameters from Model 4 are consistent with those of Model 1, where a partially absorbed power-law component does not result in a better fit (which is expected, given low levels of the extragalactic hydrogen column density, $N_{\rm H}$, found across all spectral models; see Table 1). Model 5 results in a significantly improved fit compared to Model 1, meeting our $\Delta C_{\rm stat}$ criterion. However, similar to Model 3, the posteriors returned by chain show that the preferred value for the power-law photon index Γ is nonphysical and is pegged at 1. Evaluating the spectral fits (see Figure 1), an additional soft emission component may be present within the region of extracted counts, possibly due to extended soft X-rays from hot nuclear gas. However, given the nonphysical value for Γ returned by Model 5, we accordingly assume the simple absorbed power-law fit as our best model (Model 1). We measure a 0.5–10 keV flux of $9.1^{+3.1}_{-3.9} \times 10^{-13}$ erg s^{-1}, corresponding to a 2–10 keV luminosity of $6.1^{+1.4}_{-2.0} \times 10^{44}$ erg s^{-1} at $z = 1.53$. In Figure 1 we show the X-ray spectrum of SDSS J0252−0028, along with the fits from Model 1 and Model 5. We list the best-fit values for model parameters in Table 1.

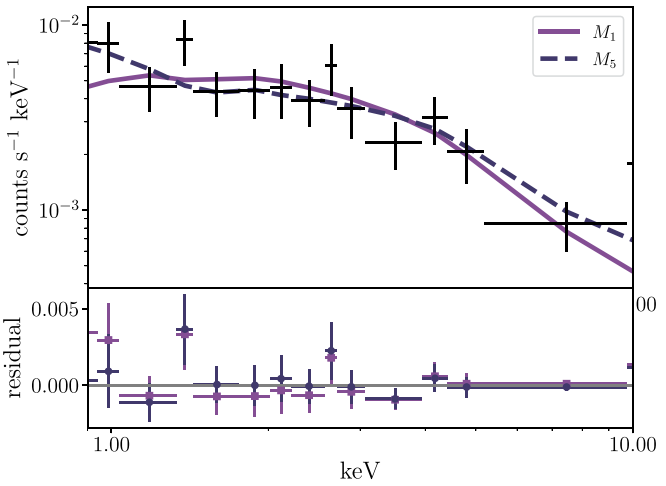

Figure 1. The rest-frame XMM-Newton spectrum for SDSS J0252−0028 (top). The spectrum has been rebinned via the specgroup tool to ensure a minimum signal-to-noise ratio of 2 over observed-frame 0.3–10 keV band. We show best fits for both Model 1 (an absorbed redshifted power law—phabs × zphabs × zpow) and Model 5 (a power law with diffuse gas—phabs × ((zphabs × zpow) +APEC)). Although Model 5 results in a significantly improved fit compared to Model 1, the posteriors returned by chain show that the preferred value for the power-law photon index Γ is nonphysical. An additional soft emission component may be present within the region of extracted counts, such as extended soft X-rays from hot nuclear gas. Given the nonphysical value for Γ returned by Model 5, we accordingly assume the simple absorbed power-law fit as our best model (Model 1). We measure a 0.5–10 keV flux of $9.1^{+3.1}_{-3.9} \times 10^{-13}$ erg s^{-1}, corresponding to a 2–10 keV luminosity of $6.1^{+1.4}_{-2.0} \times 10^{44}$ erg s^{-1} at $z = 1.53$.

Table 1
XMM-Newton Spectral Fits

Model (1)	$N_{\rm H}$ (2)	Γ_1 (3)	Γ_2 (4)	kT (5)	$N_{\rm fp}$ (6)	$C_{\rm stat}$ (7)
1	$<10^{-2}$	$1.5^{+1.0}_{-0.5}$	...	...	3	41.4
2	$<10^{-2}$	$1.5^{+0.8}_{-0.5}$	$1.5^{+0.8}_{-0.5}$	...	4	41.4
3	$<10^{-2}$	$1.1^{+1.8}_{-0.1}$	$2.8^{+0.2}_{-1.7}$	...	5	37.1
4	$<10^{-2}$	$1.5^{+0.8}_{-0.4}$	$1.5^{+0.8}_{-0.4}$	...	4	41.4
5	$<10^{-2}$	$1^{+1.9}_{-0}$	...	$1.2^{+8.8}_{-0.5}$	5	35.6

Note. Columns: (1) Model number, where Model 1 is an absorbed redshifted power law (phabs × zphabs × zpow), Models 2 and 3 are an absorbed redshifted broken power law (phabs × zphabs × zbknpow, where the photon index values are tied for Model 2), Model 4 is a partially covered power law (phabs × (zphabs × zpow) +zpow), and Model 5 is a power law with diffuse gas (phabs × (zphabs × zpow) +APEC); (2) the best-fit extragalactic column density in units of 10^{22} cm^{-2}; (3) the best-fit spectral index for Γ_1; (4) the best-fit spectral index for Γ_2 (only relevant for Model 3); (5) the best-fit spectral value for kT (only relevant for Model 5); (6) the number of free parameters for a given model; (7) the Cash statistic for the best fit. Error bars represent the 95% confidence level of each distribution.

3. Multiwavelength SED

In the following section, we construct a multiwavelength SED of SDSS J0252−0028 (see also Liao et al. 2021, where this data set is first presented). Similar to the analysis presented

Table 2
Multiwavelength Luminosity Values

Filter/Detector (1)	Telescope/Survey (2)	$\log \nu$ (3)	$\log \nu L_\nu$ (4)
C-band	VLA	9.78	39.98 ± 0.63
W4	WISE	13.5	<45.76
W3	WISE	13.8	<45.28
W2	WISE	14.2	44.99 ± 0.11
W1	WISE	14.4	44.96 ± 0.24
J	UKIDSS	14.5	45.21 ± 0.05
K	UKIDSS	14.7	45.16 ± 0.06
H	UKIDSS	14.8	44.94 ± 0.07
z	SDSS	14.93	45.17 ± 0.14
i	SDSS	15.00	45.34 ± 0.39
r	SDSS	15.01	45.35 ± 0.23
g	SDSS	15.21	45.36 ± 0.24
u	SDSS	15.32	45.45 ± 0.31
NUV	GALEX	15.52	44.12 ± 0.45
FUV	GALEX	15.69	<43.50
EPIC pn	XMM-Newton	18.16	$44.79^{+0.55}_{-0.50}$
...	NuSTAR	19.04	<46.02

Note.—Columns: (1) Filter or detector; (2) Telescope or survey; (3) rest-frame frequency assuming a redshift of $z = 1.53$, in units of hertz. The XMM-Newton and NuSTAR frequency corresponds to the central rest-frame frequency of their respective observing ranges (i.e., 6 and 45 keV); (4) extinction- and *K*-corrected luminosity assuming a luminosity distance $D_L = 11.36$ Gpc, in units of erg s^{-1}. Please see the text for details on extinction values and *K*-corrections applied.

in Foord et al. (2017), we combine all available multiwavelength observations and compare the SED to the standard nonblazar AGN SEDs presented in Shang et al. (2011). To correct for the effective narrowing of the filter width with redshift, we adopt the *K*-correction relation as presented in Richards et al. (2006). In particular, the $K(z)$ relation for a power-law continuum is given by $K = -2.5(1 + \alpha_\nu)\log(1 + z)$, assuming $F_\nu \propto \nu^{-\alpha_\nu}$.

The available SED observations include a radio flux measurement from the Karl G. Jansky Very Large Array (Thompson et al. 1980), where the rest-frame 6 GHz luminosity is measured in Chen et al. (2021); archival mid-infrared (MIR) photometry from WISE (Wright et al. 2010); archival near-infrared (NIR) photometry from UKIDSS (Lawrence et al. 2007); archival optical photometry from SDSS (York et al. 2000); and archival UV photometry from GALEX (Martin et al. 2005). We correct the archival MIR–UV magnitudes for extinction using dust maps from Schlafly & Finkbeiner (2011) and reddening curves from Fitzpatrick (1999). *K*-corrections are then applied assuming values of $\alpha = -1.0$, -0.5, and -1.57, for the IR, optical, and UV measurements (Ivezić et al 2002; Richards et al. 2006; Shang et al. 2011). We also include our X-ray observations from XMM-Newton (Jansen et al. 2001) and NuSTAR (Harrison et al. 2013). The luminosities for each rest-frame frequency are listed in Table 2.

In Figure 2 we plot the full multiwavelength SED of SDSS J0252−0028 where, following the normalization procedure in Shang et al. (2011), the flux density of our data is normalized to $\lambda \approx 4200$ Å. This value is estimated by interpolating between our bluest UKIDSS data point, at rest-frame $\lambda \approx 4934$ Å, and our reddest SDSS data point, at rest-frame $\lambda \approx 3530$ Å. A simple comparison between the data and the Shang et al. (2011) SED shows a good agreement between the emission of SDSS J0252−0028 and that of a radio-quiet AGN. However, there is a clear deficit of emission from SDSS J0252−0028 between the NIR and UV frequencies, with a large drop in emission near 1400 Å. Furthermore, given the FUV GALEX upper limit at rest-frame ∼600 Å, it is possible that the slope of the drop is larger than presented in Figure 2.

3.1. Comparison to Binary AGN Accretion Models

This drop in emission in the SED may be a result a binary AGN accretion mode. In particular, if SDSS J0252−0028 is a binary AGN system with separation $a = 200\ R_S$ (where $R_S = 2GMc^{-2}$ is the Schwarzchild radius for a black hole with mass *M*), as estimated in Liao et al. (2021), the binary is well into the gravitational-wave dominated regime. Here, circumbinary accretion is likely and we may expect that individual accretion disks have formed around each SMBH. In such a scenario, any radiation that a standard accretion disk would radiate between the inner edge of the circumbinary disk and the tidal truncation radii of the minidisks will be missing. This missing emission can produce a notch in the thermal continuum spectrum (e.g., Gültekin & Miller 2012; Kocevski et al. 2012; Roedig et al. 2012; Tanaka et al. 2012; Tanaka & Haiman 2013; Roedig et al. 2014; and see Farris et al. 2015b for simulations where notches become obscured).

Following a procedure similar to that outlined in Foord et al. (2017), we use the analytical calculations derived in Roedig et al. (2014) to analyze how the SED shape is affected by the presence of a notch. In particular, we model the specific luminosity integrated from the circumbinary disk and the two minidisks assuming that the primary and secondary BHs are accreting at rates $\dot{M}_{\rm pri} = f_{\rm pri}\dot{M}$ and $\dot{M}_{\rm sec} = f_{\rm sec}\dot{M}$. Here, $\dot{M}_{\rm pri}$ and $\dot{M}_{\rm sec}$ are the mass accretion rates of the primary and secondary, and $\dot{M}$ is the circumbinary accretion rate. These calculations assume that the circumbinary disk is in inflow equilibrium, such that $f_{\rm pri} + f_{\rm sec} = 1$. Values of $f_{\rm pri}$ and $f_{\rm sec}$ depend on the mass ratio of the system, *q*, and simulations have shown that for most values of mass ratio, $f_{\rm sec} > f_{\rm pri}$ (but as *q* increases toward equal mass, the accretion rate ratio goes to unity; see Farris et al. 2014).

Hydrodynamical simulations of circumbinary accretion disks around binary SMBHs with a range of mass ratios ($0.026 < q < 1.0$) have shown that significant periodicity in the accretion rates occurs only at $q > 0.1$ (Farris et al. 2014). At these mass ratios, the binary torques are strong enough to lead to periodicity in the accretion rates, and thus the light curve of the system. Previously, the light curves of SDSS J0252−0028 were modeled with both $q = 0.11$ and $q = 0.43$ (two mass ratio regimes probed by Farris et al. 2014); however, the fits to the data did not strongly prefer one model over the other, and a value of $q = 0.11$ was adopted to interpret the results (Liao et al. 2021).

In Figure 2 we show two examples of SED models with notches for both $q = 0.11$ and $q = 0.43$. Here, we adopt the predicted $f_{\rm pri}$ and $f_{\rm sec}$ values expected for each mass ratio as estimated in Farris et al. (2014). As evident, as the mass ratio decreases and the secondary's accretion rate dominates, the notch occurs at shorter wavelengths and deepens; this is a result of the primary SMBH's accretion flow barely contributing to the total SED (Roedig et al. 2014). Because we do not expect significant modulation in the accretion rates at $q < 0.1$, our mass ratio model of $q = 0.11$ represents the lowest and deepest notch expected for this system. We find that this model is unable to match the shape of SDSS J0252−0028's SED, and in

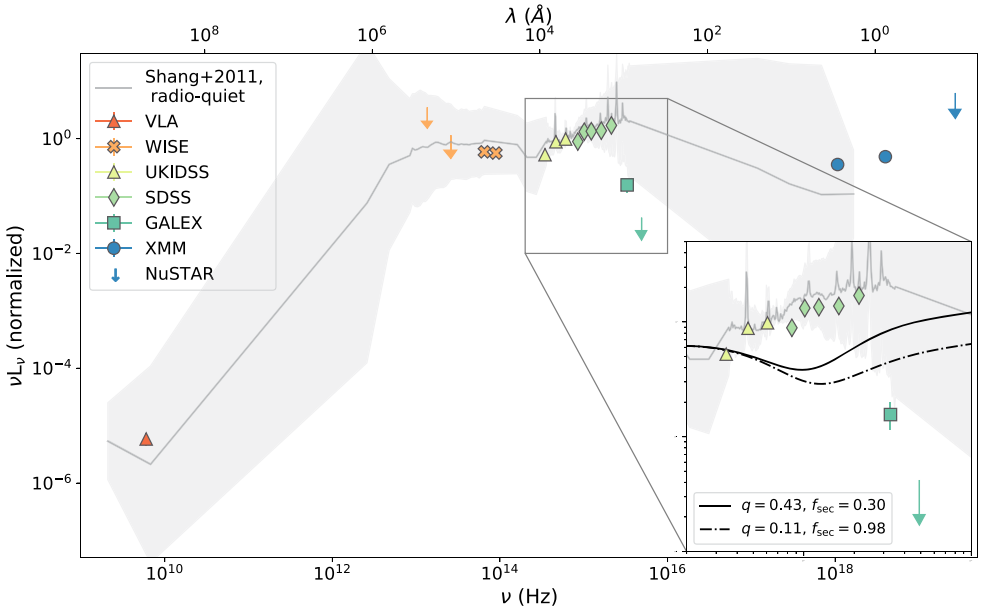

Figure 2. The rest-frame multiwavelength SED of SDSS J0252−0028. We plot the radio flux density upper limit from VLASS (red pentagon), MIR photometry from WISE (orange "x" markers for the W2 and W1 filter detections, and upper limits for the W3 and W4 filters), NIR photometry from UKIDSS (yellow triangles), optical photometry from SDSS (green diamonds), UV photometry from GALEX (dark green square for the NUV detection, and upper limit for the FUV), and X-ray photometry from XMM-Newton (dark blue circles) and NuSTAR (upper limit). In gray we overplot the composite nonblazar radio-quiet quasar SED from Shang et al. (2011). In general we find a good agreement between the SED of SDSS J0252−0028 and that of the composite quasar SED. However, SDSS J0252−0028 appears to have a deficit of emission between the NIR and FUV bands, significantly dropping off near ∼1400 Å. In the inset we show various models for a possible "notch" in the accretion disk of a binary AGN, with different mass ratios (q) and accretion rates for the primary, $f_{\rm pri}$, and secondary, $f_{\rm sec}$ (where $f_{\rm pri}+f_{\rm sec}=1$; see Section 3.1 for more details). Although lower values of q and higher values $f_{\rm sec}$ will result in a deeper and wider notch, we find that the most extreme values fail to accurately capture the FUV GALEX upper limit.

particular predicts a lower level of emission in the range rest-frame 1400−3500 Å (SDSS) and a higher level of emission at $\lambda < 1400$ Å (GALEX) than observed.

Lastly, disregarding the mass ratio constraint of $q > 0.1$ for significant accretion modulation, extremely low (high) values of q ($f_{\rm sec}$) can further deepen the notch to potentially match the GALEX data points. However the size of the notch will also widen—resulting in larger differences between the predicted and observed rest-frame optical and NUV emission (UKIDSS and SDSS observations; see Figure 2).

3.1.1. Enhanced Hard X-Ray Emission

Many computational results on binary mergers indicate that binary SMBHs should have enhanced hard X-ray emission relative to a single SMBH (Roedig et al. 2014; Farris et al. 2015b; Ryan & MacFadyen 2017; d'Ascoli et al. 2018; Tang et al. 2018), a result of supersonic streams from the circumbinary disk shocking at the minidisk edges. Yet, results from these simulations have a wide range in the predicted energy at which these enhancements should occur, from tens of keV up to over 100 keV. Although Roedig et al. (2014) predict a Wien-like spectrum may adequately describe the emission, the large range of possible peak temperatures does not allow us to carry out an in-depth analysis of a possible hot-spot X-ray contribution to the multiwavelength SED.

However, using the derivations presented in Roedig et al. (2014), we can estimate an approximate peak temperature of an additional Wien-like spectrum by calculating the postshock temperature, $T_{\rm ps}$, which is proportional to the binary's semimajor axis, a, and mass ratio, q: $T_{\rm ps} \propto (a/50R_S)^{-1} \times (1+q^{0.7})^{-1}$ (see Roedig et al. 2014 for more details). We consider possible temperatures for the stream-shocking emission from SDSS J0252−0028, given an assumed semimajor axis $a = 200\,R_S$ and a range of q values between 0.1 and 1.0. Adopting the assumption presented in Roedig et al. (2014) that a mass ratio $q = 1.0$ and semimajor axis $a = 50\,R_S$ will result in an additional Wien-like spectrum with peak energy 100 keV, we estimate that excess emission from hot spots in SDSS J0252−0028 could peak at rest-frame 25–42 keV, or observed-frame 10–16 keV. Although our XMM-Newton observation falls below this energy window, the spectrum shows no evidence of excess hard X-ray emission with respect to an absorbed power-law model. Furthermore, our NuSTAR upper limit does not allow us to assess the presence of enhanced hard X-ray emission at higher energies. Additional studies of the hard X-ray emission associated with binary AGNs (especially in the unequal-mass regime) will allow for more rigorous hard X-ray analyses of binary AGN candidates in the future.

Lastly, we note that the enhanced X-ray emission expected from binary AGNs raises the possibility of binaries having different X-ray spectral indices (see Section 2 for our analysis of the X-ray spectrum) or optical to X-ray spectral indices ($\alpha_{\rm ox}$; see, e.g., Yuan et al. 1998; Vignali et al. 2003; Strateva et al. 2005; Steffen et al. 2006; Just et al. 2007; Kelly et al. 2008; Lusso et al. 2010) than single AGNs. This ratio is defined as $\alpha_{\rm ox} = -\log[L_{2\,\rm keV}/L_{2500}]/2.605$, and has been shown to strongly correlate with the optical luminosity of the AGN at 2500 Å (e.g., Silverman et al. 2005; Lusso et al. 2010). We estimate the approximate rest-frame 2500 Å flux density using the available SDSS r-band photometry (which corresponds to rest-frame emission at ≈2440 Å), and we use the XMM-Newton fit results from Model 1 (see Section 2) to estimate the 2 keV flux density. We calculate $\alpha_{\rm ox} \approx 1.6$, consistent within

the error of the range expected from a single AGN with similar 2500 Å luminosities (see Lusso et al. 2010).

4. Possible Causes of Reddening

In the following section we discuss alternative physical explanations for the observed multiwavelength SED of SDSS J0252−0028, which is not well explained by either a standard AGN or a binary AGN system. In particular, we investigate whether the effects of reddening can match the steep drop-off seen near ∼1400 Å.

The unusual SED of SDSS J0252−0028, with infrared and optical emission typical of an AGN but strongly cut off through the near-UV, is similar to (albeit less extreme than) the SED of contentious binary AGN candidate Mrk 231 (see Smith et al. 1995; Veilleux et al. 2013; Leighly et al. 2014; Yan et al. 2015; Leighly et al. 2016). The binary AGN hypothesis proposed for Mrk 231 is that the smaller-mass black hole accretes as a thin disk, dominating the weak UV emission, while the larger-mass black hole radiates inefficiently as an Advection Dominated Accretion Flow, and both are surrounded by a circumbinary disk (dominating the optical and IR emission). Here, emission blueward of the near-UV is dominated by accretion onto the smaller-mass black hole and thus the SED is expected to have a steep drop-off toward the UV, near the inner edge of the circumbinary disk (Yan et al. 2015).

However, it has been shown that the unusual shape is consistent with circumstellar reddening (Leighly et al. 2014), and that if the observed FUV continuum is intrinsic, it fails by a factor of 100 to power the observed strength of the near-infrared emission lines (Leighly et al. 2016). Most recently, Guo et al. (2020) studied the effects of reddening on a large sample of binary SMBH candidates that were targeted due to their light-curve periodicities. Similar to Leighly et al. (2014), they found that dust reddening was a possible explanation for systems with significant drops in emission throughout the IR–UV SED.

Following the logic presented in Leighly et al. (2014), we apply a reddening correction from Fitzpatrick (1999) to the composite radio-quiet quasar SED from Shang et al. (2011) to fit the photometric data points of SDSS J0252−0028 between rest-frame 87300 Å and 910 Å (i.e., the WISE, UKIDSS, SDSS, and NUV GALEX data points). We fit for the best values of A_V and $R(V)$ via the `python` nonlinear least-squares fitting package `lmfit`. In addition to the reddening relation presented in Fitzpatrick (1999), we also use the analytical correction presented in Goobar (2008), which assumes a spherical scattering medium (and used by Leighly et al. 2014 when analyzing Mrk 231). Although this reddening law is typically used to describe low values of $R(V)$ around Type Ia supernovae, a spherical geometry with significant optical depth (and multiple scatterings) allows for the removal of more blue photons from the line of sight than a screen. Both extinction models are calibrated for wavelengths between the IR and UV bands. In particular, the Goobar (2008) parameterization was developed from Monte Carlo simulations of light propagation down to 3600 Å, while the Fitzpatrick (1999) relations are appropriate for wavelengths greater than 1150 Å. We extrapolate both relations to include the GALEX NUV data point (rest-frame 910 Å); although it is hard to know whether the models will describe this region of wavelength space precisely, the scattering opacity generally increases toward blue wavelengths. Work has been done that suggests the far-UV rise should continue down to a wavelength of 950 Å (e.g., Snow et al. 1990). Lastly, we note that at X-ray energies (>1 keV) the photoelectric cross section (or, at higher energies, the Thompson cross section) should dominate interactions. Thus, we do not expect that the reddening laws modeled by Goobar (2008) and Fitzpatrick (1999) are applicable for our X-ray data points, but instead are fit for in XSPEC via the `zphabs` parameter.

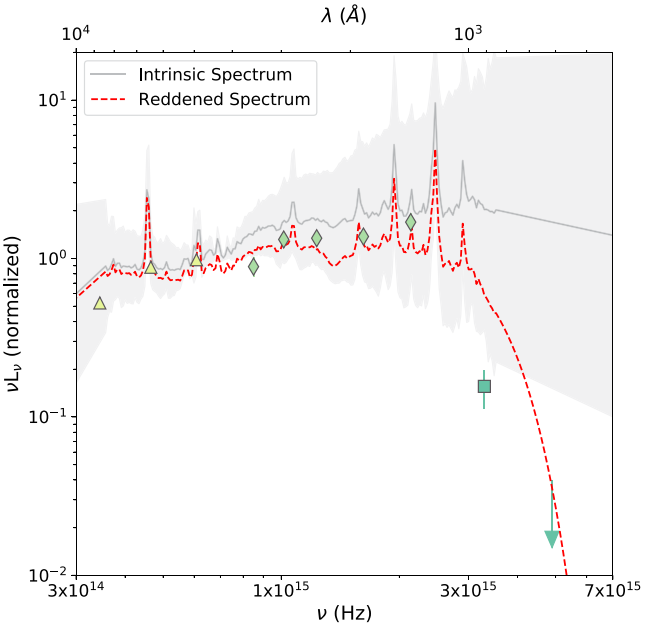

Figure 3. The best-fit reddened spectrum (red dashed line) when fitting the composite radio-quiet SED from Shang et al. (2011; gray line) to the photometric data points of SDSS J0252−0028 (between rest-frame 87300 Å and 610 Å). We plot NIR photometry from UKIDSS (yellow triangles), optical photometry from SDSS (green diamonds), and UV photometry from GALEX (dark green square for the NUV detection, and upper limit for the FUV). We apply the reddening law from Fitzpatrick (1999), although we find consistent results when using the reddening law presented in Goobar (2008; which has been used in past analyses of binary AGN candidate Mrk 231). We find best-fit values of $A_V = 0.17$ and $R(V) = 2.54$. Overall, once accounting for circumstellar reddening, the composite single quasar spectrum agrees well with the measured emission of SDSS J0252−0028.

The best-fit results of both reddening laws are consistent within the errors, although the reddening correction from Fitzpatrick (1999) yields a slightly better fit (as determined from the Bayesian information criterion values). We find best-fit values of $A_V = 0.17$ and $R(V) = 2.54$. In Figure 3 we plot the results of our best-fit reddened quasar SED along with the photometric data points from the SED of SDSS J0252−0028. With the addition of circumstellar reddening, the composite quasar spectrum agrees well with the measured emission of SDSS J0252−0028. The best-fit $R(V)$ value is indicative of dust similar to that in the Milky Way (where $R(V) \sim 3.1$).

Multiwavelength follow-up of binary SMBH candidates is an important step to better identify the accretion nature of AGNs with periodic light curves. At face value, the predicted detection rate of binary SMBHs from the DES-SN analysis (Chen et al. 2020; Liao et al. 2021) has been higher than theoretical predictions (e.g., Haiman et al. 2009; Volonteri et al. 2009; Graham et al. 2015; Kelley et al. 2019). However, because the theoretical predictions are tailored to populations of SMBH binaries that differ from the sensitivities of the DES-SN, the best comparison between theory and observations may

be a differential detection rate (i.e., as a function of redshift and black hole mass). A thorough discussion of the discrepancy between the observational results and theoretical predictions are presented in Chen et al. (2020).

Lastly, although we find the SED of SDSS J0252−0028 is best described by a single AGN obscured by circumstellar dust, it is possible that the system is a binary where a notch has been masked by (1) circumstellar dust, (2) the tail end of a Wien-like spectrum that peaks at hard (>10 keV) energies, or (3) a combination of both. Follow-up spectroscopy in the IR, which is relatively free of the effects of reddening, can help determine whether circumstellar reddening is acting on its own. For example, Leighly et al. (2016) analyze observed He I ($\lambda = 10830$ Å), Pβ ($\lambda = 12818$ Å), Pα ($\lambda = 18751$ Å), and C IV ($\lambda = 1549$ Å) emission lines of Mrk 231 with Cloudy to show that the measured equivalent widths and emission-line ratios in the IR are not reproducible with the binary AGN model proposed by Yan et al. (2015).

5. Conclusions

In this work we present a multiwavelength analysis of binary AGN candidate SDSS J0252−0028. SDSS J0252−0028 was part of a large systematic search for long-term periodic light curves in 625 quasars, and was flagged as a binary AGN candidate based on a significant periodicity measured in 20 yr SDSS–DES data (Chen et al. 2020; Liao et al. 2021). New X-ray observations via XMM-Newton and NuSTAR, along with available radio (VLA), MIR (WISE), NIR (UKIDSS), optical (SDSS), and UV (GALEX) observations, have been combined to search for evidence of two accreting SMBHs. The main results and implications of this work can be summarized as follows.

1. We analyze new X-ray observations of SDSS J0252−0028 (obtained with NuSTAR and XMM-Newton). We find no emission consistent with an X-ray point source within 100″ of the SDSS-listed optical center of SDSS J0252−0028 when analyzing the NuSTAR data. We calculate a 3σ upper limit for 3–10 keV and 10–79 keV fluxes of 8.8×10^{-14} erg s^{-1} and 67×10^{-14} erg s^{-1}, respectively. We identify the quasar as an X-ray point source in the XMM-Newton observation and search for evidence of two accreting SMBHs by fitting the observed-frame 0.5–10 keV spectrum with five different models. Although an additional soft emission component may be present within the region of extracted counts, a simple absorbed power law remains the best-fit model, as expected from a single AGN. We measure a 0.5–10 keV flux of $9.1^{+3.1}_{-3.9} \times 10^{-13}$ erg s^{-1}, corresponding to a 2–10 keV luminosity of $6.1^{+1.4}_{-2.0} \times 10^{44}$ erg s^{-1} at $z = 1.53$.
2. We combine all available multiwavelength observations and compare the SED to a standard nonblazar AGN SED. The available SED observations include a radio flux measurement from the VLA, MIR photometry from WISE, NIR photometry from UKIDSS, optical photometry from SDSS, and UV photometry from GALEX. We find a good agreement between the SED of SDSS J0252−0028 and that of a standard AGN; however, there is a clear deficit of emission from SDSS J0252−0028 between the optical and UV frequencies, with a large drop in emission near rest-frame 1400 Å.
3. We investigate whether the drop in emission in the SED may be a result of circumbinary accretion, where individual disks have formed around each SMBH. Using analytical calculations derived in Roedig et al. (2014), we analyze how the SED of a standard quasar could be affected by the presence of a notch. However, even at the most extreme values of mass ratios and accretion rates, we find the model is unable to match the shape of SDSS J0252−0028's SED.
4. We estimate an approximate peak temperature of an additional Wien-like spectrum in the hard X-rays, as a result of possible stream shocking in a binary AGN system. We find that excess emission from hot spots in SDSS J0252−0028 could peak at rest-frame 25–42 keV, or observed-frame 10–16 keV. Although our XMM-Newton observation falls below this energy window, the spectrum shows no evidence of excess hard X-ray emission with respect to an absorbed power-law model. Furthermore, our NuSTAR upper limit does not allow us to detect the presence of enhanced hard X-ray emission at higher energies. We search for other evidence of enhanced X-ray emission by analyzing α_{OX}, and calculate a value of 1.6, consistent within the error of the range expected from a single AGN.
5. We investigate whether the effects of circumstellar reddening can match the steep drop-off in the multiwavelength SED near 1400 Å. Following the logic presented in Leighly et al. (2014), we apply a reddening correction from Fitzpatrick (1999) to a standard nonblazar AGN SED to fit the photometric data points of SDSS J0252−0028 between rest-frame 87300 Å and 610 Å. With the addition of circumstellar reddening, the standard quasar spectrum agrees well with the measured emission of SDSS J0252−0028. We find best-fit values of $A_V = 0.17$ and $R(V) = 2.54$.

We have shown through various analyses that there is an absence of evidence supporting SDSS J0252−0028 as a binary AGN system. However, given the small number of currently confirmed binary AGNs, the best method to distinguish a binary AGN from a single AGN is consistently changing. These studies are further complicated by the fact that analyses searching for signs of circumbinary accretion will likely be dependent on the unique parameters of a given binary AGN system. For SDSS J0252−0028, future observations of IR emission lines can be used to better understand whether a binary AGN accretion model is able to account for the emission seen at longer wavelengths. Overall, hard X-ray emission signatures may be the most telling sign of circumbinary accretion—however, current results from simulations are extremely model dependent (with a wide range of predicted energies where enhancements should occur). A more rigorous analysis of the binary AGN hypothesis for SDSS J0252−0028 can be made with future studies of the expected hard X-ray emission associated with binary AGNs (especially in the unequal-mass regime).

A.F. acknowledges support by the Porat Postdoctoral Fellowship at Stanford University. X.L. and Y.C.C. acknowledge support by NSF grant AST-2108162 and NASA grant 80NSSC21K0060. Y.C.C. acknowledges support by the government scholarship to study abroad from the ministry of education of Taiwan and the Illinois Survey Science Graduate Student Fellowship. NuSTAR is a project led by the California Institute of Technology (Caltech), managed by the Jet Propulsion Laboratory (JPL), and funded by the National Aeronautics and Space Administration (NASA). We thank the NuSTAR Operations, Software, and Calibrations teams for

support with these observations. This research has made use of the NuSTAR Data Analysis Software (NuSTARDAS) jointly developed by the ASI Science Data Center (ASDC, Italy) and the California Institute of Technology (Caltech, USA). This work is also based on observations obtained with XMM-Newton, an ESA science mission with instruments and contributions directly funded by ESA Member States and NASA. This work makes use of data obtained as part of the Karl G. Jansky Very Large Array (VLA), UKIRT Infrared Deep Sky Survey (UKIDSS), Wide-field Infrared Survey (WISE), Sloan Digital Sky Survey (SDSS), and the Galaxy Evolution Explorer (GALEX). The National Radio Astronomy Observatory is a facility of the National Science Foundation operated under cooperative agreement by Associated Universities, Inc. WISE is a joint project of the University of California, Los Angeles, and the Jet Propulsion Laboratory/California Institute of Technology, funded by the National Aeronautics and Space Administration. GALEX is a NASA Small Explorer, launched in 2003 April. We acknowledge NASA's support for construction, operation, and science analysis for the GALEX mission, developed in cooperation with the Centre National d'Etudes Spatiales of France and the Korean Ministry of Science and Technology. Some of the data presented in this paper were obtained from the Mikulski Archive for Space Telescopes (MAST) at the Space Telescope Science Institute. The specific observations analyzed can be accessed via doi:10.17909/t9-bqed-ab26 and doi:10.17909/t9-p4qg-dd43. Lastly, this research has made use of NASA's Astrophysics Data System.

Facilities: NuSTAR - The NuSTAR (Nuclear Spectroscopic Telescope Array) mission, XMM-Newton X-Ray Multimirror Mission satellite, VLA, WISE, UKIDSS, SDSS, GALEX.

Software: NuSTARDAS, SAS (v18.0.0; Gabriel et al. 2004), XSPEC (v12.11.1; Arnaud 1996).

ORCID iDs

Adi Foord https://orcid.org/0000-0002-1616-1701
Xin Liu https://orcid.org/0000-0003-0049-5210
Kayhan Gültekin https://orcid.org/0000-0002-1146-0198
Kevin Whitley https://orcid.org/0000-0001-9379-6519
Fangzheng Shi https://orcid.org/0000-0003-3922-5007
Yu-Ching Chen https://orcid.org/0000-0002-9932-1298

References

Arnaud, K. A. 1996, in ASP Conf. Ser., 101, Astronomical Data Analysis Software and Systems V, ed. V. Systems, G. H. Jacoby, & J. Barnes, 17
Begelman, M. C., Blandford, R. D., & Rees, M. J. 1980, Natur, 287, 307
Bon, E., Zucker, S., Netzer, H., et al. 2016, ApJS, 225, 29
Brightman, M., Nandra, K., Salvato, M., et al. 2014, MNRAS, 443, 1999
Brightman, M., & Ueda, Y. 2012, MNRAS, 423, 702
Burke-Spolaor, S., Taylor, S. R., Charisi, M., et al. 2019, A&ARv, 27, 5
Cash, W. 1979, ApJ, 228, 939
Charisi, M., Bartos, I., Haiman, Z., et al. 2016, MNRAS, 463, 2145
Chen, Y.-C., Liu, X., Liao, W.-T., et al. 2020, MNRAS, 499, 2245
Chen, Y.-C., Liu, X., Liao, W.-T., & Guo, H. 2021, MNRAS, 507, 4638
d'Ascoli, S., Noble, S. C., Bowen, D. B., et al. 2018, ApJ, 865, 140
Deane, R. P., Paragi, Z., Jarvis, M. J., et al. 2014, Natur, 511, 57
Dey, L., Gopakumar, A., Valtonen, M., et al. 2019, Univ, 5, 108
D'Orazio, D. J., Haiman, Z., & MacFadyen, A. 2013, MNRAS, 436, 2997
Dotti, M., Colpi, M., Haardt, F., & Mayer, L. 2007, MNRAS, 379, 956
Farris, B. D., Duffell, P., MacFadyen, A. I., & Haiman, Z. 2014, ApJ, 783, 134
Farris, B. D., Duffell, P., MacFadyen, A. I., & Haiman, Z. 2015a, MNRAS, 446, L36
Farris, B. D., Duffell, P., MacFadyen, A. I., & Haiman, Z. 2015b, MNRAS, 447, L80
Fitzpatrick, E. L. 1999, PASP, 111, 63
Foord, A., Gültekin, K., Reynolds, M., et al. 2017, ApJ, 851, 106
Gabriel, C., Denby, M., Fyfe, D. J., et al. 2004, in ASP Conf. Ser., 314, Astronomical Data Analysis Software and Systems (ADASS) XIII, ed. F. Ochsenbein, M. G. Allen, & D. Egret (San Francisco, CA: ASP), 759
Gold, R., Paschalidis, V., Etienne, Z. B., Shapiro, S. L., & Pfeiffer, H. P. 2014, PhRvD, 89, 064060
Goobar, A. 2008, ApJL, 686, L103
Graham, M. J., Djorgovski, S. G., Stern, D., et al. 2015, Natur, 518, 74
Gültekin, K., & Miller, J. M. 2012, ApJ, 761, 90
Guo, H., Liu, X., Zafar, T., & Liao, W.-T. 2020, MNRAS, 492, 2910
Haiman, Z., Kocsis, B., & Menou, K. 2009, ApJ, 700, 1952
Hardee, P. E., Cooper, M. A., & Clarke, D. A. 1994, ApJ, 424, 126
Harrison, F. A., Craig, W. W., Christensen, F. E., et al. 2013, ApJ, 770, 103
Hayasaki, K., Mineshige, S., & Sudou, H. 2007, PASJ, 59, 427
Hooper, E. J., Impey, C. D., Foltz, C. B., & Hewett, P. C. 1995, ApJ, 445, 62
Ishibashi, W., & Courvoisier, T. J.-L. 2010, A&A, 512, A58
Ivezić, Ž. , Menou, K. , Knapp, G. R. , et al 2002, AJ, 124, 2364
Jansen, F., Lumb, D., Altieri, B., et al. 2001, A&A, 365, L1
Just, D. W., Brandt, W. N., Shemmer, O., et al. 2007, ApJ, 665, 1004
Kaastra, J. S. 2017, A&A, 605, A51
Kellermann, K. I., Condon, J. J., Kimball, A. E., Perley, R. A., & Ivezić, Ž. 2016, ApJ, 831, 168
Kelley, L. Z., Haiman, Z., Sesana, A., & Hernquist, L. 2019, MNRAS, 485, 1579
Kelly, B. C., Bechtold, J., Trump, J. R., Vestergaard, M., & Siemiginowska, A. 2008, ApJS, 176, 355
Khan, F. M., Berentzen, I., Berczik, P., et al. 2012, ApJ, 756, 30
Kocevski, D. D., Faber, S. M., Mozena, M., et al. 2012, ApJ, 744, 148
Lawrence, A., Warren, S. J., Almaini, O., et al. 2007, MNRAS, 379, 1599
Leighly, K. M., Terndrup, D. M., Baron, E., et al. 2014, ApJ, 788, 123
Leighly, K. M., Terndrup, D. M., Gallagher, S. C., & Lucy, A. B. 2016, ApJ, 829, 4
Li, Y.-R., Wang, J.-M., Ho, L. C., et al. 2016, ApJ, 822, 4
Liao, W.-T., Chen, Y.-C., Liu, X., et al. 2021, MNRAS, 500, 4025
Liu, X., Hou, M., Li, Z., et al. 2019, ApJ, 887, 90
Luo, J., Chen, L.-S., Duan, H.-Z., et al. 2016, CQGra, 33, 035010
Lusso, E., Comastri, A., Vignali, C., et al. 2010, A&A, 512, A34
MacFadyen, A. I., & Milosavljević, M. 2008, ApJ, 672, 83
Martin, D. C., Fanson, J., Schiminovich, D., et al. 2005, ApJL, 619, L1
Mayer, L., Kazantzidis, S., Madau, P., et al. 2007, Sci, 316, 1874
Merritt, D., Mikkola, S., & Szell, A. 2007, ApJ, 671, 53
Milosavljević, M., & Phinney, E. S. 2005, ApJL, 622, L93
Muñoz, D. J., Lai, D., Kratter, K., & Miranda, R. 2020, ApJ, 889, 114
Paczynski, B. 1977, ApJ, 216, 822
Richards, G. T., Strauss, M. A., Fan, X., et al. 2006, AJ, 131, 2766
Rodriguez, C., Taylor, G. B., Zavala, R. T., et al. 2006, ApJ, 646, 49
Roedig, C., Krolik, J. H., & Miller, M. C. 2014, ApJ, 785, 115
Roedig, C., Sesana, A., Dotti, M., et al. 2012, A&A, 545, A127
Ryan, G., & MacFadyen, A. 2017, ApJ, 835, 199
Schlafly, E. F., & Finkbeiner, D. P. 2011, ApJ, 737, 103
Sesana, A., Haardt, F., & Madau, P. 2007, ApJ, 660, 546
Shang, Z., Brotherton, M. S., Wills, B. J., et al. 2011, ApJS, 196, 2
Silverman, J. D., Green, P. J., Barkhouse, W. A., et al. 2005, ApJ, 618, 123
Smith, P. S., Schmidt, G. D., Allen, R. G., & Angel, J. R. P. 1995, ApJ, 444, 146
Snow, T. P., Allen, M. M., & Polidan, R. S. 1990, ApJL, 359, L23
Steffen, A. T., Strateva, I., Brandt, W. N., et al. 2006, AJ, 131, 2826
Strateva, I. V., Brandt, W. N., Schneider, D. P., Vanden Berk, D. G., & Vignali, C. 2005, AJ, 130, 387
Tanaka, T., Menou, K., & Haiman, Z. 2012, MNRAS, 420, 705
Tanaka, T. L., & Haiman, Z. 2013, CQGra, 30, 224012
Tang, Y., Haiman, Z., & MacFadyen, A. 2018, MNRAS, 476, 2249
Thompson, A. R., Clark, B. G., Wade, C. M., & Napier, P. J. 1980, ApJS, 44, 151
Tozzi, P., Gilli, R., Mainieri, V., et al. 2006, A&A, 451, 457
Valtonen, M. J., Lehto, H. J., Nilsson, K., et al. 2008, Natur, 452, 851
Vaughan, S., Uttley, P., Markowitz, A. G., et al. 2016, MNRAS, 461, 3145
Veilleux, S., Trippe, M., Hamann, F., et al. 2013, ApJ, 764, 15
Vignali, C., Brandt, W. N., & Schneider, D. P. 2003, AJ, 125, 433
Volonteri, M., Miller, J. M., & Dotti, M. 2009, ApJL, 703, L86
Wright, E. L., Eisenhardt, P. R. M., Mainzer, A. K., et al. 2010, AJ, 140, 1868
Yan, C.-S., Lu, Y., Dai, X., & Yu, Q. 2015, ApJ, 809, 117
York, D. G., Adelman, J., Anderson, J. E. J., et al. 2000, AJ, 120, 1579
Yuan, W., Siebert, J., & Brinkmann, W. 1998, A&A, 334, 498